Journal of Applied Electrochemistry (2005) 35:915–924
DOI 10.1007/s10800-005-4720-y

Effect of preparation procedure of IrO_2–Nb_2O_5 anodes on surface and electrocatalytic properties

MÀRIO H.P. SANTANA[1], LUIZ A. DE FARIA[1] and JULIEN F.C. BOODTS[2,*]
[1]*Departamento de Química - FFCLRP/USP, Av. Bandeirantes, 3900, CEP 14040-901, Ribeirão Preto/SP, Brasil*
[2]*Instituto de Química, Universidade Federal de Uberlândia, Av. João Naves de Ávila, 2160, Uberlândia/MG 38400-902, Brasil*
*(*author for correspondence, fax: +055-34-3239-4208, e-mail: jfcboodts@ufu.br)*

Received 10 April 2004; accepted in revised form 21 March 2005

Key words: electrocatalytic properties, iridium oxide, niobium oxide, oxygen, ozone, preparation procedure

Abstract

The influence of the electrode manufacturing procedure on surface and electrocatalytic properties for oxygen and ozone evolution at electrodes of nominal composition Ti/[IrO_2–Nb_2O_5] (45:55 mol%) was investigated. Thermal decomposition at 450 °C (1 h, air stream) was adopted as standard procedure. Metal support pretreatment, solvent mixture, method of applying the precursor mixture and calcination procedure were all investigated. X-ray diffraction, scanning electronic microscopy, voltammetric and differential capacity analysis show the use of HCl 1:1 as solvent and applying the mixture by brush led to fragile rugged/porous oxide coatings. However, for the same conditions, but controlled calcination (heating/cooling rates), the coating becomes more compact. Using isopropanol as solvent results in a more homogeneous coating, presenting the lowest morphology factor. Kinetic investigation shows the rugged/porous coating presents the lowest Tafel slopes and the highest global electrocatalytic activity for OER. The more compact the coating the lower the electrochemically active surface area and the global OER activity. Ozone efficiency depends on the electrochemically active area while support pretreatment strongly influences the lifetime of the electrode. Application of a Pt interlayer between the oxide and Ti base improves the service life.

1. Introduction

The nature of the electrode material is one of the most important features to deal with in order to achieve high efficiency for electrochemical ozone production, EOP [1–5]. An appropriate electrode material should present good conductivity and resistance to anodic corrosion and a high anodic overpotential for the oxygen evolution reaction, OER. Besides, electrolyte anions and cations should not engage in competitive reactions with OER/EOP and hydrogen evolution reaction, HER, respectively. Therefore, the vast majority of EOP investigations [1, 2, 5–7] make use of Pt, glassy carbon, and PbO_2 as electrode materials. EOP investigations using DSA® -type electrodes are rather scarce and were firstly studied by Foller and Tobias [1]. Recently, we showed Ti/[IrO_2–Nb_2O_5] anode is able to generate ozone with reasonable current efficiency, although its lifetime was rather limited [4].

Another important aspect about materials for EOP investigations is the electrode morphology. In previous work, we demonstrated the degree of porosity/roughness of the oxide structure strongly affects EOP efficiency [2, 4]. Since electrode morphology, electrocatalytic properties and lifetime of oxide anodes are interrelated, it is a delicate task to improve one aspect without making worse another. So a balance between the several variables involved should be found. It is well known metal substrate pretreatment, decomposition temperature, precursor mixture solvent and coating composition all influence the oxide properties.

In a previous paper [4], we demonstrated the best electrode composition for EOP is IrO_2–Nb_2O_5 (45:55 mol%). In the present paper, thermal decomposition at 450 °C (1 h, air stream) was maintained as the basic preparation procedure, investigating the influence of parameters such as: Ti support pretreatment, precursor mixtures solvent, method of applying the precursor mixture and the annealing procedure of the coatings. All of these parameters were investigated in terms of surface properties, kinetics and electrocatalytic properties for OER/EOP processes.

Table 1. Electrode codes according to the preparation procedure adopted

Code	Ti-support pretreatment	Precursor solvent	Method of applying precursor mixture to the Ti support[a]
A	Blasted with steel micro-spheres	HCl 1:1 (v/v)	[1] Painted; partial calcinations for 10 min; 1 h final calcination (thermal shock[2])
B	Ditto	isopropanol	Ditto
C	Polished with emery paper (#120)	HCl 1:1 (v/v)	[3] Application of a single drop with a micro-pipette; heating rate: 7°C min^{-1}; calcinated for 1 h; cooling rate: 2°C min^{-1}
D	Blasted with steel micro-spheres	HCl 1:1 (v/v)	Ditto
E	The same as sample D, but with a Pt interlayer deposited between Ti-support and oxide coating		

[a] For all samples, solvent was evaporated at 80 °C before calcination.

[1] Painting by brush and partial calcinations at 450 °C repeated until oxide load $\cong$ 1.5 mg cm^{-2} was reached.

[2] Electrode taken out of the furnace immediately at the end of annealing time.

[3] Volume calculated from the concentration of the precursor mixture and the desired oxide load.

2. Experimental

2.1. *Electrode preparation*

IrO_2–Nb_2O_5 (45:55 mol%) anodes (duplicate samples) were prepared by thermal decomposition (450 °C, 1 h, air stream) of 0.18 mol dm^{-3} chloride precursor mixtures applied to a titanium support (5 × 10 × 0.15 mm). The Ti support was degreased with isopropanol and submitted to chemical attack (10 min) with boiling oxalic acid (10% w/w). Precursor mixtures were applied to both faces of the Ti support, dried at 80 °C and the residue calcinated in air. In some electrodes (A and B, see Table 1), the precursor mixture was applied by brushing and calcinated for 10 min. (3–4 repetitions), while for others (C, D and E), the calculated volume of the mixture was applied with a micro-pipette. These latter electrodes were calcinated using controlled heating/cooling rates. The conditions used in the preparations of the several IrO_2–Nb_2O_5 anodes are gathered in Table 1. In all cases, a 2 μm nominal coating thickness, corresponding to a 1.54 mg oxide loading, was used. The theoretical oxide loading is calculated taking into account the percentage of each oxide, its density and the volume of the active layer and the real load determined by weighing.

2.2. *Cell*

A three-compartment all-glass cell (0.2 dm^3) was used throughout. Ohmic drop was minimised using a Luggin capillary, while two heavily platinised platinum wires acted as counter electrodes. Electrode potentials were read against a reversible hydrogen electrode (RHE) containing the base electrolyte, BE, (3.0 mol dm^{-3} H_2SO_4).

2.3. *Techniques/equipment*

Electrodes were characterised by XRD using a Siemens D5000 instrument with CuK_α radiation (1.5406 Å). SEM analysis were done with a ZEISS DSM 940A equipment.

E_{oc} of freshly prepared electrodes was read 15 min after their immersion in the electrolyte (0.5 mol dm^{-3} H_2SO_4). Voltammetric profiles (i vs. E) were recorded at 20 mV s^{-1} covering the 0.4–1.4 V (vs. RHE) pseudo-capacitive potential interval. Morphology factor (ϕ) and capacity data (C) were obtained following the procedure recently proposed by Da Silva et al. [8], which consists in recording 20 consecutive voltammetric curves covering the 1.2 to 1.35 V (RHE) pseudo-capacitive potential interval. The total (internal + external), C_T, and external (more easy to access surface regions of the coating), C_E, capacity values were obtained from the slope of the two straight segments in the i_c vs. v -plot, observed in the low and high v -domains, respectively. Current data were measured close to $E_{\lambda,\ a}$ at 1.33 V (RHE). The internal capacity (more difficult to access surface regions, e.g. microcracks, pores, inter-granular contacts), C_I, was calculated using next relation: $C_I = C_T - C_E$. The morphology factor, ϕ, was calculated according to $\phi = C_I/C_T$ (for more details see ref. [8]).

Kinetic data were obtained recording polarisation curves under quasi-stationary conditions (1 mV s^{-1}) covering the 0.1–300 mA cm^{-2} current density interval, using BE with and without 0.03 mol dm^{-3} KPF_6. Ozone production was investigated under galvanostatic conditions using a current density of 0.8 A cm^{-2} at 0 °C. Ozone concentration in the N_2 carrier gas, used to transport O_3 from the electrolytic cell (anodic compartment) to the spectrophotometer, was analysed on line by UV absorption at 254 nm. Current efficiency data were calculated according to the following equation [2]:

$$\Phi_{EOP}/\% = [(A\overset{o}{V}zF)/(l\varepsilon I_T)]100 \qquad (1)$$

where: A = Absorbance at 254 nm; $\overset{o}{V}$ = volumetric flow rate of (N_2 + O_2 + O_3) ($\mathrm{dm}^3\ \mathrm{s}^{-1}$); z = number of electrons ($z = 6$) ε = ozone absorptivity at 254 nm (3024 $\mathrm{cm}^{-1}\ \mathrm{mol}^{-1}\ \mathrm{dm}^3$ [9]); l = optical path (10 cm); I_T = total current (EOP + OER) (Ampere);

Φ_{EOP} = current efficiency for EOP (%); F= Faraday's constant (96485 C mol^{-1}).

All solutions were prepared volumetrically using twice distilled water with a final pass through a Millipore Milli–Q$_{plus}$ apparatus. Fluka "purum" products were used throughout. An AUTOLAB (Eco Chemie, The Netherlands), model PGSTAT20, was used throughout. Temperature control was done by means of a model FC55A01 FTS cooling system.

3. Results and discussion

3.1. *Surface Analysis*

Figure 1 shows a representative low angle XRD spectrum. All spectra present well-defined Ti° peaks, attributed to the X-ray beam reaching the metallic support.

The spectra denunced an amorphous phase together with much smaller and less defined IrO_2 peaks when compared to crystalline IrO_2 (JCPDS 43-1019). No Nb_2O_5 peaks are observed. Figure 1 suggests low sinterization, with small crystallites and no solid solution formation. Such structure is related to the high Nb_2O_5 content (55 mol %), an amorphous oxide at the preparation conditions used [4, 10, 11]. At 450 °C, IrO_2 normally forms the rutile crystalline phase [11–13]. However, due to accentuated $NbCl_5$ hydrolysis [4] (an oxide whose behaviour is very similar to $TaCl_5$ [13, 14]), IrO_2-based coatings are amorphous, resulting in IrO_2–Nb_2O_5 films composed of IrO_2 microparticles dispersed in the amorphous Nb_2O_5 phase [4, 13, 15]. The IrO_2 peaks at $2\theta = 34.5°$ and 53.4° are somewhat more intense and sharper for sample C, a result consistent with the controlled heating/cooling rate used during calcination (without thermal shock) of this sample. This leads to a more complete precursor decomposition and growth of larger crystallites (lower roughness/porosity).

Representative SEM micrographs are presented in Figure 2. All coatings show the cracked mud morphology consisting of large crystallites (presenting flat areas) separated by cracks.

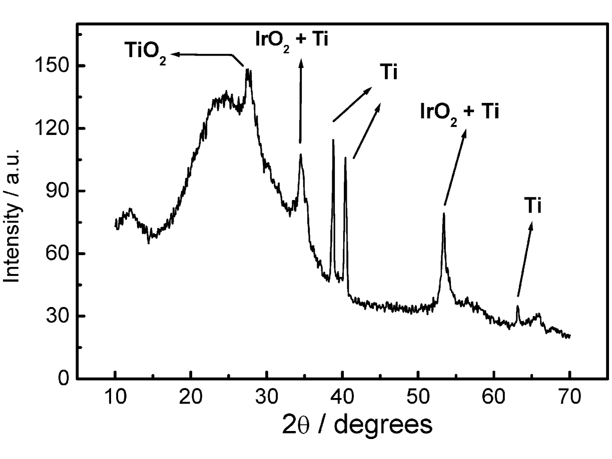

Fig. 1. Representative low angle XRD spectrum of sample C (see Table 1 for identification).

Small grains, which were identified as IrO_2 aggregates in other investigations [13, 15, 16], can also be observed. Despite those common aspects, sample A presents a more heterogeneously cracked structure, with a higher number of defects, deeper and large cracks if compared to samples B and C, while the structure of sample B consists of more homogeneously distributed and smaller cracks. This difference can be attributed to the change in solvent and is in agreement with XRD analysis and literature data [17]. Confirming the XRD analysis, sample C presents much larger flat areas and fewer cracks due to the controlled slow calcination/cooling rates used. Since the calcination/cooling step used for this sample (and for samples D and E) results in a longer heat treatment, the crystallites grow and separate in a way the cracks can reach the support (see Figure 2d). Such observation is very interesting since the deactivation process of these DSA® -type electrodes involves the passivation of the metallic support. So, a possible way to minimise passivation is the deposition of a Pt interlayer between the support and the oxide layer (sample E).

3.2. *Open circuit potential and voltammetric curves*

Representative voltammetric profiles recorded using standard conditions ($v = 20$ mV s^{-1}, $\Delta E = 0.4$–1.4 V/RHE; 0.5 mol dm^{-3} H_2SO_4) are shown in Figure 3.

The voltammetric profile is the typical electrochemical spectrum of the Ir(III)/Ir(IV) ($E° = 0.93$ V/RHE) solid state surface redox transition (SSSRT), normally observed for IrO_2-based electrodes [4, 18–20], and is

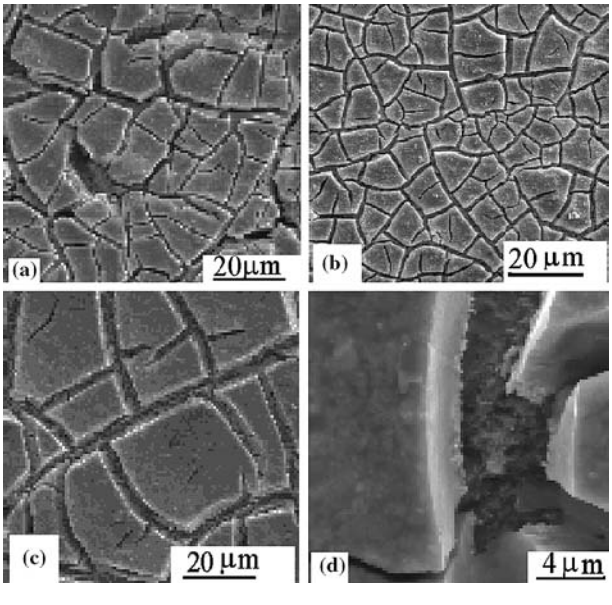

Fig. 2. SEM micrographs of IrO_2–Nb_2O_5 (45:55 mol%) of samples manufactured using different preparation procedures. Amplification of 1000 X: (a) sample A; (b) sample B; (c) sample C. Amplification of 5,000 X: (d) sample E.

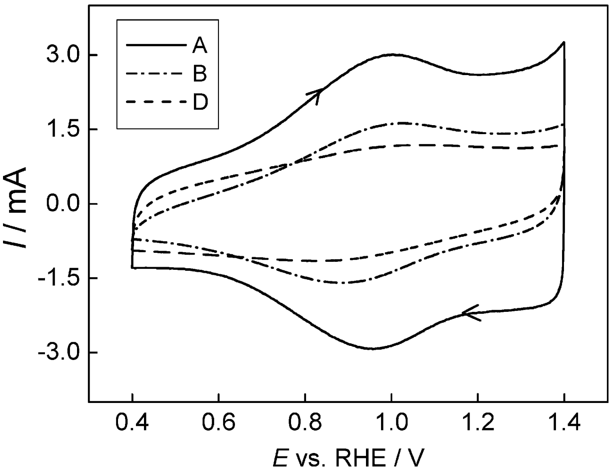

Fig. 3. Voltammetric curves of IrO_2–Nb_2O_5 (45:55 mol%) samples (see legend). Electrolyte: 0.5 mol dm^{-3} H_2SO_4; $v = 20$ mV s^{-1}; $T = 25°C$.

independent on the pretreatment of the Ti support. Samples C, D and E present lower currents and no clearly defined redox transition peaks, contrary to samples A and B. This behaviour can be attributed to the more extensive sinterization during the slow controlled heating/cooling step, thus reducing the electrochemically active surface area (EASA) [21]. Samples A and B, whose preparation involves a thermal shock, show defined peaks and higher current densities (see Figure 3) supporting the coatings present a greater number of cracks, pores (higher EASA) [4, 15]. Comparing samples A and B, the use of an organic solvent (isopropanol – sample B) reduces about twice the current density (more compact coatings are obtained). This corroborates our previous discussion (see topic 3.1) and Angelinetta et al. [17] findings.

E_{oc} measurements showed two distinct behaviours as a function of the solvent used: $E_{oc} = 0.96$ V (RHE) for HCl 1:1 and $E_{oc} = 1.04$ V for isopropanol. Since E_{oc}-values reflect changes in the equilibrium surface Ir(III)/Ir(IV) ratio and this redox couple governs the surface electrochemistry [22], using the Nernst equation, the surface active site ratios were calculated being: $a_{Ir(IV)} \cong 3\ a_{Ir(III)}$ (solvent: HCl 1:1); $a_{Ir(IV)} \cong 70\ a_{Ir(III)}$ (solvent: isopropanol). These values reflect the influence of the solvent on the surface composition of mixed oxides. Roginskaya and Morozova [13] concluded the phase composition of an oxide system is determined by the interactions of the species formed during the hydrolytic stage of coating preparation. Charged colloid formation, due to precursor hydrolysis ($NbCl_5$), and charged complex species ($[IrCl_6]^{-2/-3}$ [12]) are important to control the surface composition. Literature data [13, 14] show in aqueous solutions Ir – and to a greater extent Ta and Nb – hydrolyse while the aqua-hydroxochloro complexes present a tendency to condense and polymerise. In such a system, calcination is particularly difficult affecting the complete oxidation of the active sites [4]. On the other hand, in organic solvents, metallic salts are not (or weakly) hydrolysed and do not easily form species such as $[IrCl_6]^{-2/-3}$ and positively charged Nb colloidal species. This favours complete precursor decomposition and oxidation, explaining the higher Ir^{+4} surface concentration of samples prepared using isopropanol as solvent.

Figure 4 shows the anodic voltammetric charge, q_a, of as-prepared electrodes obtained by integration of the anodic branch of the voltammetric profiles, as function of electrode manufacturing.

Considering q_a is due to double layer charging + SSSRT, its value is proportional to the EASA [23]. Comparison of the data of Figure 4 shows metallic support pretreatment, solvent, method of precursor application and the use of a Pt-interlayer all have minor influence on the EASA. The significant difference in q_a of sample A can be traced back to the thermal shock this sample received during its preparation. However, the influence of thermal shock can be avoided if an organic solvent (sample B – isopropanol) is used. Samples prepared using controlled heating/cooling rates present a more compact oxide layer. This electrode manufacturing procedure furnishes more time for the crystallites to growth and accommodate, thus reducing the number of cracks provoked by a thermal shock [24].

3.3. *Surface characterisation by differential capacity and morphology factor, ϕ*

Ex situ characterisation of surface porosity by nitrogen adsorption [25] is executed under drastically different conditions from the reality of an electrochemical experiment. In contrast, *in situ* voltammetric characterisation furnishes important information about the degree of electrode roughness and the portion of the electrode surface accessible to the electrolyte (inner and outer surface), permitting calculation of the "electrochemical porosity" [2, 23], described here by the morphology factor [4, 8, 26].

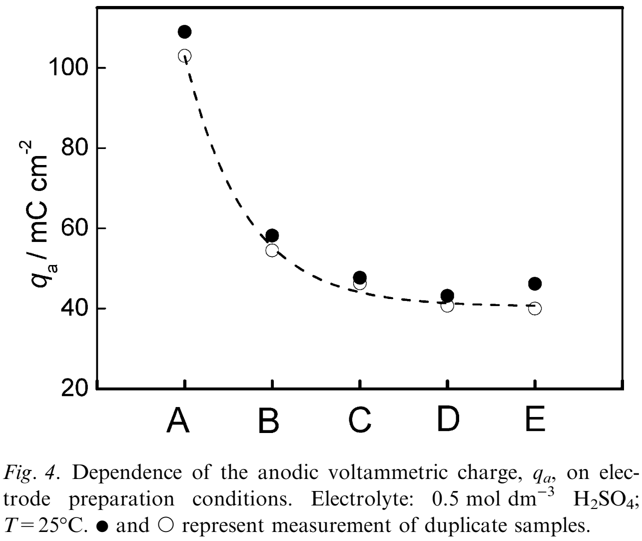

Fig. 4. Dependence of the anodic voltammetric charge, q_a, on electrode preparation conditions. Electrolyte: 0.5 mol dm^{-3} H_2SO_4; $T = 25°C$. ● and ○ represent measurement of duplicate samples.

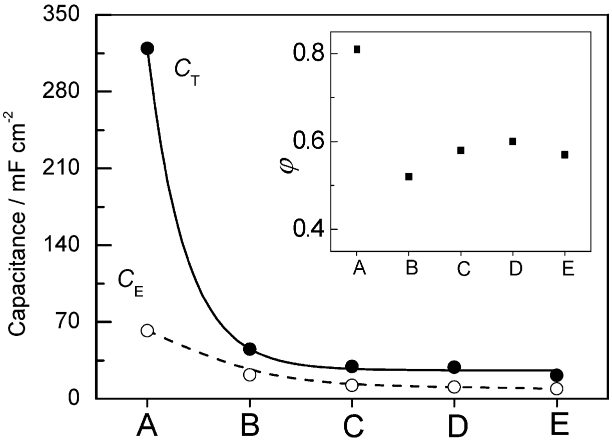

Fig. 5. Dependence of surface parameters (C_T, C_E and ϕ (inset)) on electrode preparation procedure. Electrolyte: 3.0 mol dm^{-3} H_2SO_4; $T = 25°C$.

Figure 5 gathers the total, C_T, and external, C_E, differential capacities and ϕ as a function of the electrode preparation procedure. Figure 5 shows the total (C_T) and external (C_E) capacities present the same behaviour as q_a (compare Figure 4). The classic preparation procedure (HCl 1:1, painting, thermal shock) gives a much more rugged/porous oxide layer with high C_T, C_I and ϕ -values. These high ϕ and C_I-values indicate the oxide morphology of sample A permits a strong contribution of the inner surface to the electrochemical response. For all other preparation variables investigated, coatings show an almost identical contribution of the internal and external surfaces to the total surface. The data also support the use of an organic solvent (sample B) in balancing out the effect of thermal shock.

Comparing samples A with C, D and E (samples prepared with the same solvent, but different method of applying the precursor mixture and/or calcination), a dramatic reduction of C_T and C_E is observed for samples not submitted to thermal shock (C, D and E). For all the results discussed up to now, the electrode preparation procedure of samples (C, D, E) alters the coating structure, increasing the sinterization and thus decreasing the surface area. These results are in complete agreement with the results of SEM and XRD characterisation. Once more, pretreatment of the Ti support does not significantly influence the surface area of the samples C, D and E, as was also observed for q_a measurements (Figure 4).

3.4. *Kinetic investigation*

Depending on their coating structures, electrodes with the same nominal composition may present different electrode kinetics. So, in principle, an influence of electrode preparation procedure on the Tafel coefficient is possible. Tafel curves were recorded under quasi steady state conditions ($v = 1$ mV s^{-1}) in 3.0 mol dm^{-3} H_2SO_4 in the presence and absence of 0.03 mol dm^{-3} KPF_6 at 25 °C. Figure 6 shows a representative Tafel curve before and after IR_Ω correction. All experimental Tafel curves showed in the high overpotential domain a deviation from linearity, thus requiring correction for ohmic drop, IR_Ω.

The raw data were corrected for IR_Ω by the procedure originally proposed by Shub and Reznik [27]. For both supporting electrolytes and the several samples investigated, R_Ω-values ($= R_{solution} + R_{film}$) in the 0.1 to 0.6 Ω range were obtained, in excellent agreement with literature [2, 4, 28] and suggest that the main contribution to R_Ω comes from the solution. After IR_Ω-correction, Tafel curves showed two linear segments proving that deviation from linearity observed in the experimental curve is due to ohmic resistance combined with changes in kinetics [4, 10, 29] (e.g. change in rate determining step or in transfer coefficient). Figure 7 shows the Tafel slopes, b, as a function of electrode preparation procedure and electrolyte composition.

The Tafel slope data reveal that the kinetics of the electrode process depend on overpotential, electrode manufacture and electrolyte composition. For both electrolytes b_1-values are in good agreement with the literature [4, 15, 23], where values in the 40–60 mV interval are normally reported for IrO_2-based electrodes. The exception is sample A which has the lowest Tafel slope, around 30 mV, but such a value has been reported at highly rugged electrodes [30], which is the case of sample A (see q_a, C and ϕ data). For IrO_2–Ta_2O_5 electrodes prepared under similar manufacturing conditions of sample C and D, Da Silva et al. [31] obtained a b_2-value of 200 mV, in the high current density domain, in excellent agreement with our b_2-values.

The introduction of PF_6^- into the electrolyte does not affect the kinetics in the low overpotential domains (b_1) for all samples investigated. This is in agreement with the literature [4, 29], which reports that addition of fluoroanions only affects the Tafel slope in the high overpotential domain. Such behaviour can be attributed to the dependence of PF_6^- adsorption on potential, which is more accentuated at higher overpotentials [2, 32]. Dif-

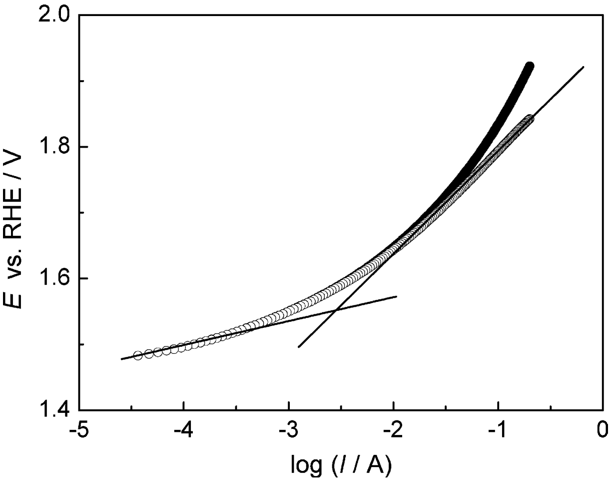

Fig. 6. Representative Tafel curve before (●) and after (○) IR_Ω-correction. Sample B. Electrolyte: 3.0 mol dm^{-3} H_2SO_4. $T = 25$ °C.

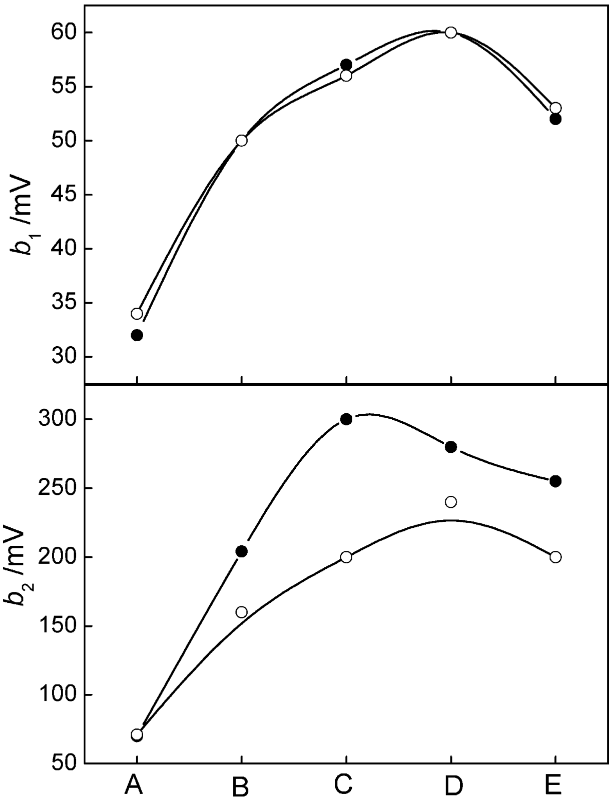

Fig. 7. Tafel slopes in the low (b_1) and high (b_2) overpotential domains as function of electrode preparation procedure. (○) BE; (●) BE + 0.03 mol dm^{-3} KPF$_6$; $T=25$°C.

ferently from the other samples, for sample A, PF_6^- does not affect the Tafel slope at high overpotentials. The lower b-values for sample A indicate its rate determining step (rds) at high overpotentials is a chemical step, different from the other electrodes (see mechanism below).

An electrode mechanism for OER/EOP at Ti/IrO_2–Nb_2O_5 electrodes was recently proposed by us [4]. Based on the experimentally observed dependence of the Tafel coefficient on the electrode preparation procedure, we propose, in order to take into account of the influence of electrode morphology, a slight modification of the mechanism recently proposed by Da Silva et al. [31].

Kinetic control steps	b/mV ($\alpha=0.5$, $T=25$ °C)	
$\equiv S+H_2O \rightarrow \equiv S–OH^*+H^+ +e^-$	120	(a)
$\equiv S–OH^* \rightarrow \equiv S–OH$	60	(b)
$\equiv S–OH \rightarrow \equiv S–O+H^+ +e^-$	40	(c)
Efficiency control steps		
$\equiv S–O \rightarrow [1-\theta] \equiv S–O+\theta \equiv S^*–O$	$0 < \theta < 1$	(d)
$[1-\theta]2 \equiv S–O \rightarrow [1-\theta]2 \equiv S–O_2$	15	(e)
$[1-\theta]2 \equiv S–O_2 \rightarrow [1-\beta]\cdot[1-\theta]2 \equiv S–O_2$ $+\beta\,[1-\theta]2 \equiv S^*–O_2$	$0 < \beta < 1$	(f)
Oxygen evolution		
$[1-\beta]\cdot[1-\theta]2 \equiv S-O_2 \rightarrow O_2 \nearrow$		(g)
Ozone formation		
$\theta \equiv S^* - O + \beta[1-\theta]2 \equiv S^* - O_2$ $\rightarrow [\theta+\beta(1-\theta)]3 \equiv S - O_3$	10	(h)
$[\theta+\beta(1-\theta)]3 \equiv S - O_3 \rightarrow O_3 \nearrow$		(i)

≡ S is an active surface site. "θ" and "β" are the partial surface concentrations describing the competition between the OER and EOP processes while "*" represents the surface coverage by oxygenated species leading to O_3-formation.

In the low overpotential domain, the anodic current is sustained by the rearrangement of the intermediate (step b). Step a being a chemical one, in principle it is not affected by PF_6^- . According to the above mechanism and considering the experimental Tafel coefficients, at low overpotentials, the 30 mV slope obtained for sample A indicates a change in mechanism [30].

$$2 \equiv S - OH \rightarrow 2 \equiv S + H_2O + 1/2\,O_2 \quad (b = 30\,\text{mV}) \tag{j}$$

Step (j) represents a recombination of the intermediate formed after the primary discharge that may occur on surfaces with a high active site concentration [33], which is the case for sample A. According to the theoretical treatment proposed by Filoche and Sapoval [34], for an elementary act of electron transfer at rugged electrodes, the dependence of Tafel slope on electrode morphology finds its origin in the non-uniform distribution of the surface electric field.

Steps (d)–(f) describe the influence of the nature of the electrode/electrolyte interface on the electrode process [2]. The current efficiency for the *EOP* process, Φ_{EOP}, depends on the surface concentration of the active centres leading to O_3-formation described by $[\theta+\beta(1-\theta)]$. This relation shows that an increase in Φ_{EOP}-value is verified when experimental conditions used increase the surface concentration of the active centres leading to *EOP*.

At high overpotentials step (a) becomes the rds, while O_3-formation, via step (h), which is only observed for $i \geqslant 0.4$ A cm^{-2}, cannot be rate determining since it is rapid and controlled by diffusion [35]. Considering primary water discharge as the rds and applying the kinetic treatment proposed by Bockris [36], the corresponding Tafel coefficient is given by:

$$b = 2.303RT/\alpha F \tag{2}$$

where α is the apparent (effective) transfer coefficient for the non ideal case [2, 4, 37]. All other parameters have their usual meaning. For the ideal α-value of 0.5 [36–39], at 25 °C, Equation (2) leads to $b=120$ mV. Comparing this theoretical value with the experimental b_2-values (see Figure 7), a discrepancy of the vast majority of the experimental b_2-slopes is observed. According to the literature [34, 39], the ideal transfer coefficient of 0.5 is only obtained for cases involving a one electron transfer process on a flat electrode surface in the absence of specific anion adsorption. The apparent α-values calculated from eq. 2, at $T=25$ °C, using the experimental b_2 Tafel slope data are shown in Figure 8 as function of electrode preparation procedure and electrolyte composition.

Sample A was excluded from Figure 8 since its Tafel slope at high overpotentials does not support primary water discharge as rds. On the contrary, this very rugged electrode gives $b_2=70$ mV, which indicates step (b), or-be-it, the rearrangement of $HO^\bullet$ (spillover), as

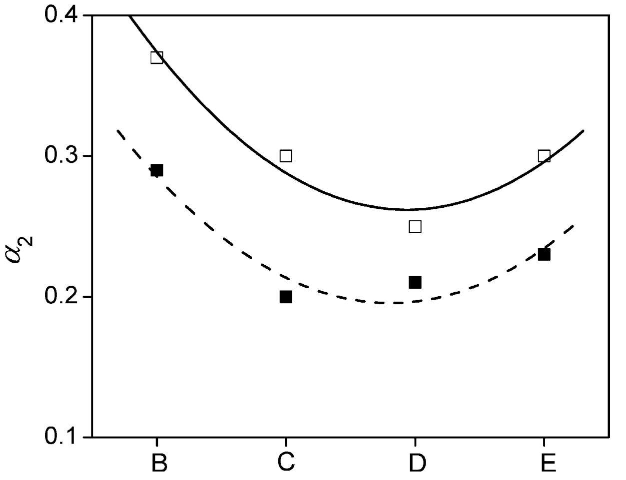

Fig. 8. Dependence of apparent transfer coefficient (calculated for the high overpotential domain) on electrode manufacturing and electrolyte. Electrolyte: 3.0 mol dm^{-3} H_2SO_4: (□) absence and (■) presence of 0.03 mol dm^{-3} KPF_6; $T = 25°C$.

the rds. This result agrees with literature data [19, 40] for mixed oxide with enhanced electrocatalytic activity for OER.

Figure 8 shows that the highest α-value is presented by the electrode with the highest total and external areas, suggesting high electrode roughness facilitates electron transfer due to a decrease in the energy barrier associated with electronic tunnelling [31, 41]. The more compact coatings have lower α-values, showing that the surface distribution of the electric field causes an increase in the activation barrier for electron transfer. As pointed out by Trasatti and Lodi [42], the transition state theory depicted by Horiuti and Polanyi [43] and by Butler [44] can be applied to metallic oxide systems. So, the behaviour shown in Figure 8 can be indeed correlated with changes in the electric component of the activation energy of the electron transfer process [2]. The influence of the electrolyte nature on α depends on electrode morphology, in agreement with other investigations [2, 31]. The influence of PF_6^- on α decreases for more compact oxide coatings. With the exception of sample A, adsorption of PF_6^- anions decreases the α-values for all samples, which according to Da Silva et al. [31], is due to the influence of competitive anion adsorption on the electron tunnelling process [45, 46].

3.5. *Electrocatalytic activity for OER*

The global electrocatalytic activity depends on both electronic and geometric factors [19, 23]. A simple way to study the global electrocatalytic activity for OER is comparing, at a fixed potential, the dependence of the current intensity on electrode manufacture and electrolyte composition [31]. Figure 9A shows the current intensity, *I*, in the high ($E = 1.85$ V) potential domain for the several samples and electrolyte compositions. *I*-values were extracted from Tafel plots already corrected for ohmic drop. The true electrocatalytic activity can be analysed by normalising the current intensity by an extensive surface parameter, thus eliminating the influence of the surface area from the electrochemical response. Since during intense gas evolution gas bubbles clog the inner coating structure (deep cracks, bottom of pores, intergranular contacts, etc) it is prudent to consider the outer surface area, described by C_E, as the effective electrochemically active surface area (see Figure 9b).

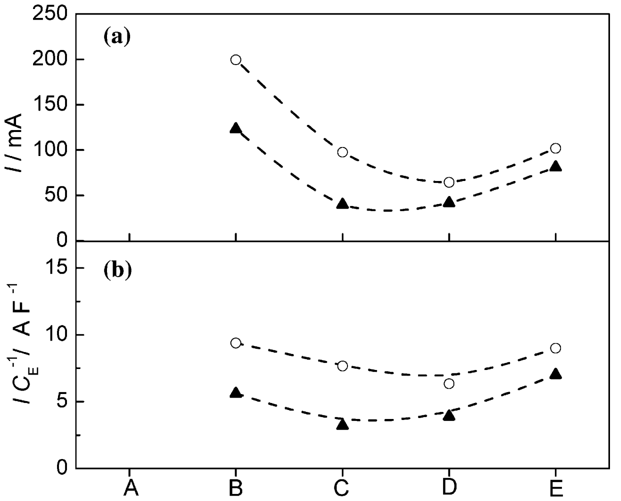

Fig. 9. Dependence of: (a) the current intensity, *I*, and (b) current intensity normalised by external area, IC_E^{-1}, on electrode manufacturing and electrolyte; *I* was measured at 1.85 V. Electrolyte: 3.0 mol dm^{-3} H_2SO_4: (○) absence and (▲) presence of 0.03 mol dm^{-3} KPF_6; $T = 25°C$.

Sample A is not shown in the high potential domain of Figure 9 since the maximum potential reached during the recording of its Tafel curves was $E = 1.64$ V, quite inferior to the other samples. In the high potential domain, an important increase in the apparent electrocatalytic activity with increasing electrochemically active surface area is observed for both electrolytes. Figure 9 also reveals a significant lower apparent and real electrocatalytic activity in the presence of KPF_6. Such findings are in agreement with the dependence of anion

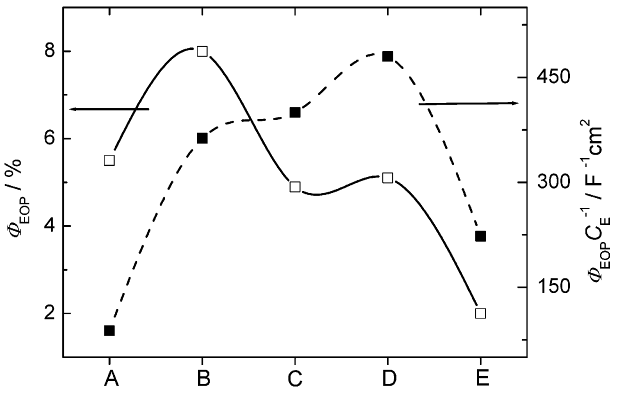

Fig. 10. Dependence of: (–□–) EOP current efficiency, Φ_{EOP}, and (–■–) normalised Φ_{EOP}-data, Φ_{EOP} C_E^{-1}, on electrode manufacturing. Electrolyte: 3.0 mol dm^{-3} H_2SO_4 + 0.03 mol dm^{-3} KPF_6; $i = 0.8$ A cm^{-2}; $T = 0$ °C.

adsorption on increasing electrode potential and demonstrates that the current efficiency for O_3 increases in the presence of fluoro-anions due to the inhibition of the OER, which is displaced to higher overpotential (see section 3.6). Identical results were obtained by Da Silva et al. [31] for IrO_2–Ta_2O_5 electrodes.

3.6. *EOP current efficiency, Φ_{EOP}*

EOP was investigated in BE + 0.03 mol dm^{-3} KPF_6, at 0 °C, at constant current density of 0.8 A cm^{-2} . Figure 10 shows the dependence of the normalised, $\Phi_{EOP}C_E^{-1}$, and non-normalised EOP current efficiency, Φ_{EOP}, on electrode manufacturing.

A detailed investigation conducted by Foller and Tobias [1] showed that O_3-production increases with increasing anode potential. This was also observed for IrO_2–Nb_2O_5 electrodes [4] up to a certain threshold potential, above which O_3-production only increases marginally. Figure 10 gathers data at $E = 7.0$ V, where Φ_{EOP}-values are maximum, showing that electrode preparation procedure strongly influences EOP performance.

In absolute terms, without normalisation, samples prepared by applying the precursor mixture by brush are the best EOP promoters, which is related to their higher active surface area and how the current density and potential is distributed in this structure. Indeed, sample A, which presents the highest C_T, C_E and ϕ data, shows a negligible EOP efficiency after normalisation, confirming this sample as the best electrocatalyst for OER. Sample B, with a more homogeneous coating structure, presents the highest global Φ_{EOP}. When normalised by the outer surface area, its EOP performance decreases, although being much higher than for sample A, whose unique difference is the solvent used in the precursor mixture.

Samples prepared with controlled heating/cooling rates (C, D and E) present small global Φ_{EOP}-values, which can be attributed to their low active surface area. When normalised by the outer surface area, samples C and D give the best EOP performance, although when compared to β-PbO_2 electrodes [1, 2, 29], IrO_2–Nb_2O_5 electrodes do not give good EOP performance. Sample E, which has a Pt interlayer, has the lowest Φ_{EOP}-values among samples C, D and E. Such small EOP performance can be explained by the lowest porosity/roughness of this oxide layer.

The performance of EOP is a function of $O^{\bullet}$ -coverage and the low Φ_{EOP}-values obtained with these DSA® materials compared to inert electrodes [1–3, 29] support the proposal that the nature of the DSA® /solution interface results in a low $O^{\bullet}$ -coverage. This, combined with a low adherence of O_2-micro bubbles due to the high wettability [23] of DSA® -type electrodes, reduces the number of effective encounters between O_2 and $O^{\bullet}$ leading to O_3 formation.

Rationalising the results, one observes that the active surface area is a key parameter in EOP. Although EOP yield is function of the active oxide area, the coating morphology must present some specific characteristics. For instance, a very rugged/porous coating such as sample A, gives a real (effective) current density much lower than the nominal I applied. Since EOP is directly related to I [1, 4], this condition leads to a very poor EOP performance. On the other hand, electrodes with very compact coatings have high specific (intrinsic) Φ_{EOP}, but the global Φ_{EOP} (non-normalised by area) is rather small.

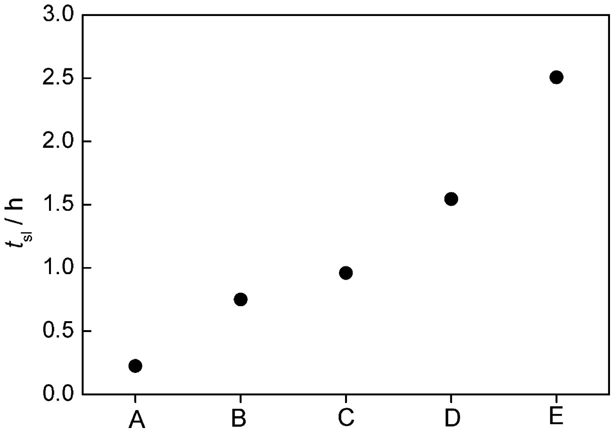

Fig. 11. Lifetime as function of electrode preparation procedure. Electrolyte: 3.0 mol dm^{-3} H_2SO_4 + 0.03 mol dm^{-3} KPF_6; $i = 0.8$ A cm^{-2} ; $T = 0$°C. Nominal oxide load: 1.54 mg cm^{-2}.

3.7. *Service life*

The service life of the samples was determined recording chronopotentiometric curves at $i = 0.8$ A cm^{-2} (0 °C). Figure 11 shows the lifetimes of all samples.

Electrode deactivation occurs due to three factors that can be associated or not: erosion, corrosion and support passivation [24, 30]. Erosion, caused by intense gas bubble formation normally operates in the early stages of the anodisation experiment when the more loosely bound particles are detached. Corrosion associated with anodic dissolution of the coating is the main process when soluble oxidation states of Ir (such as IrO_4^{2-} [24]) are formed at high overpotentials. Ti support passivation, specially deleterious for rugged/porous oxide layer, is manifested by a sudden increase in the anode potential, causing total deactivation of the anodes. This behaviour is caused by the growth of an undoped TiO_2 layer at the Ti-support/oxide interface due to Ti oxidation. Ti-support oxidation is highly dependent on the degree of protection furnished by the oxide coating. So, highly porous/rugged coatings normally have a rather low service life. It is interesting to observe that q_a as function of electrode manufacture (see Figure 4), presents the opposite behaviour of the service life, demonstrating the intimate relation with the coating roughness.

Sample A (the most porous/rugged coating) was eroded during the initial moments of the experiment (powder was noticed at the bottom of the cell). As a result, besides erosion, support passivation sets in rapidly due to electrolyte penetration through the porous structure, exposing regions of the Ti-substrate [28]. Electrodes prepared under identical conditions, but using isopropanol as solvent (sample B) have a lifetime twice that of sample A. This result is easily understood considering that its more homogeneous (compact) oxide layer presents less defects than sample A. The use of controlled heating/cooling rate influences the service life in the same direction by producing more compact coatings. A significant result is the much higher service life of the E sample where a Pt interlayer was applied giving direct Ti-support protection.

4. Conclusions

XRD showed that the coatings present low crystallinity while SEM analysis revealed that the oxide morphology strongly depends on the electrode preparation procedure. These results were corroborated by *in situ* characterisation that showed IrO_2–Nb_2O_5 electrodes prepared using HCl 1:1 as solvent combined with application of precursor mixture by painting result in porous and rugged coating presenting large active surface area. Using isopropanol as solvent the oxide coating becomes more homogeneous and less fragile. Electrodes prepared by controlled heating/cooling rates are rather compact, displaying the lowest total, external and internal surface areas. For all samples, surface electrochemistry is controlled by the Ir(III)/Ir(IV) redox couple for all samples.

Kinetic investigation showed the OER/EOP processes depend on the method of electrode manufacture. A mechanism was proposed to explain the different Tafel coefficients and the influence of electrode morphology. The high Tafel slopes observed in the high overpotential domain are attributed to anion adsorption and gas bubble adherence to the electrode surface. A decrease in the apparent transfer coefficient values was observed for more compact coatings in the BE containing KPF_6. These findings were correlated to the presence of PF_6^- in the double layer, increasing the energy barrier for the electron transfer. Investigation of the electrocatalytic activity for OER in both low and high current density domains revealed true electrode activity decreases in the presence of KPF_6 in the electrolyte with decreasing porosity/roughness of the oxide coating.

Compared to PbO_2 (the most widely used electrode material for EOP), the several DSA® electrodes manufactured do not present good EOP performance. This finds its origin in the low stability of $O^\bullet$ -coverage and/or low adherence of the O_2 micro-bubbles to the electrode surface. The EOP performance is related to the electrode morphology, being a function of the external surface area. The improvement in EOP performance observed in the presence of KPF_6 is attributed to the inhibition of the OER caused by this fluoro-compound. The lifetime of the electrodes is strongly influenced by the protection to the Ti-support furnished by the coating structures, with the highest lifetimes observed for the more compact oxide layers. Ti support passivation is a key parameter to improve the service life as supported by the significant increase of service life shown by the sample prepared with the Ti-support protected by a Pt interlayer.

Acknowledgements

Mário H. P. Santana acknowledges a Ph.D. fellowship received from the FAPESP Foundation. Julien F. C. Boodts acknowledges a Visiting Researcher Fellowship granted by the FAPEMIG Foundation.

References

1. P.C. Foller and W. Tobias, *J. Electrochem. Soc.* **129** (1982) 506.
2. L.M. Da Silva, L.A. De Faria and J.F.C. Boodts, *Electrochim. Acta* **48** (2003) 699.
3. L.M. Da Silva, M.H.P. Santana and J.F.C. Boodts, *Quím. Nova* **26** (2003) 880.
4. M.H.P. Santana, L.A. De Faria and J.F.C. Boodts, *Electrochim. Acta* **49** (2004) 1925.
5. P.C. Foller and G.H. Kelsall, *J. Appl. Electrochem.* **23** (1993) 996.
6. J.C.G. Thanos and D. Wabner, *Electrochim. Acta* **30** (1985) 753.
7. R.G. Rice and A. Netzer, *Handbook of Ozone Technology and Applications* 1 (Ann Arbor Science, England, 1982), pp. 250.
8. L.M. Da Silva, L.A. De Faria and J.F.C. Boodts, *Electrochim. Acta* **47** (2001) 395.
9. O. Leitzke, *proceedings of the Internationales Symposium Ozon und Wasser* (Germany, Berlin, 1977), pp. 164.
10. M.H.P. Santana, L.M. Da Silva and L.A. De Faria, *Electrochim. Acta* **48** (2003) 1885.
11. A.J. Terezo and E.C. Pereira, *Electrochim. Acta* **45** (2000) 4351.
12. T.A. Lassali, J.F.C. Boodts and L.O.S. Bulhões, *Electrochim. Acta* **44** (1999) 4203.
13. Yu. E. Roginskaya and O.V. Morozova, *Electrochim. Acta* **40** (1995) 817.
14. R. Mraz and J. Krysa, *J. Appl. Electrochem.* **24** (1994) 1262.
15. R. Otogawa, M. Morimitsu and M. Matsunaga, *Electrochim. Acta* **44** (1998) 1509.
16. J. Krysa, L. Kule, R. Mraz and I. Rousar, *J. Appl. Electrochem.* **26** (1996) 999.
17. C. Angelinetta, S. Trasatti, Lj.D. Atanasoska and R.T. Atanasoski, *J. Electroanal. Chem.* **214** (1986) 535.
18. S. Ardizzone, A. Carugati and S. Trasatti, *J. Electroanal. Chem.* **126** (1981) 287.
19. C.P. De Pauli and S. Trasatti, *J. Electroanal. Chem.* **538** (2002) 145.
20. Ch. Comninellis and G.P. Vercesi, *J. Appl. Electrochem.* **21** (1991) 335.
21. L.A. Da Silva, V.A. Alves, M.A.P. da Silva, S. Trasatti and J.F.C. Boodts, *Electrochim. Acta* **42** (1997) 271.
22. J. Van Muylder and M. Pourbaix. *in* M. Pourbaix (Ed), Atlas of Electrochemical Equilibria in Aqueous Solutions, (NACE International, Texas, 1974), pp. 373.
23. S. Trasatti, *Electrochim. Acta* **36** (1991) 225.
24. G.N. Martelli, R. Ornellas and G. Faita, *Electrochim. Acta* **39** (1994) 1551.
25. D.N. Furlong, D.E. Yates and T.W. Healy in Electrodes of Conductive Metallic Oxides, (edited by S. Trasatti.), Part B, (Elsevier, Amsterdam, 1981), Ch.8.

26. M.H.P. Santana, L.A. De Faria and J.F.C. Boodts, *Electrochim. Acta* **50** (2005) 2017.
27. D.M. Shub and M.F. Reznik, *Elektrokhimiya* **21** (1985) 855.
28. J.M. Hu, H.M. Meng, J.Q. Zhang and C.N. Cao, *Corros. Sci.* **44** (2002) 1655.
29. E.R. Kötz and S. Stucki, *J. Electroanal. Chem.* **228** (1987) 407.
30. S. Trasatti. *in* J. Lipkowski and P.N. Ross (Eds), The Electrochemistry of Novel Materials, (VCH-Publishers Inc., Weinheim, 1994), pp. 207.
31. L.M. Da Silva, D.V. Franco, L.A. De Faria and J.F.C. Boodts, *Electrochim. Acta* **49** (2004) 3977.
32. S. Smolinski, P. Zelenay and J. Sobkowski, *J. Electroanal. Chem.* **442** (1998) 41.
33. G. Lodi, E. Sivieri, A. De Battisti and S. Trasatti, *J. Appl. Electrochem.* **8** (1978) 135.
34. M. Filoche and B. Sapoval, *Electrochim. Acta* **46** (2000) 213.
35. A.A. Babak, R. Amadelli, A. De Battisti and V.N. Fateev, *Electrochim. Acta* **39** (1994) 1597.
36. J.O'M. Böckris, *J. Chem. Phys.* **24** (1956) 817.
37. V.M. Tsionskii, L.I. Krishtalik and L.B. Kriksunov, *Electrochim. Acta* **33** (1988) 623.
38. B.E. Conway, D.J. Mackinnon and B.V. Tilak, *Trans. Faraday Soc.* **66** (1970) 1203.
39. P. Rüetschi, *J. Electrochem. Soc.* **106** (1959) 819.
40. L.A. De Faria, J.F.C. Boodts and S. Trasatti, *J. Appl. Electrochem.* **26** (1996) 1195.
41. J. O'M. Böckris and A.K.N. Reddy: 'Modern Electrochemistry' Vol. 2, (Plenum Press, New York, 1977), Ch. 8.
42. S. Trasatti and G. Lodi, *in* S. Trasatti (Ed.), Electrodes of Conductive Metallic Oxides, Part B, (Elsevier, Amsterdam,1981), Ch.10.
43. A. Horiuti and A. Polanyi, *Acta Physicochim. USSR* **2** (1935) 505.
44. A.V. Butler, *Proc. Roy. Soc.* **157** (1936) 243.
45. A.M. Kuznetsov and J. Ulstrup, *Electrochim. Acta* **45** (2000) 2339.
46. R.R. Nazmutdinov, G.A. Tsirlina, O.A. Petrii, Y.I. Kharkats and A.M. Kuznetsov, *Electrochim. Acta* **45** (2000) 3521.